



**HAL**  
open science

## **Astrometric and photometric characterization of $\eta$ Tel B combining two decades of observations**

P. H. Nogueira, C. Lazzoni, A. Zurlo, T. Bhowmik, C. Donoso-Oliva, S. Desidera, J. Milli, S. Pérez, P. Delorme, A. Fernandez, et al.

### ► **To cite this version:**

P. H. Nogueira, C. Lazzoni, A. Zurlo, T. Bhowmik, C. Donoso-Oliva, et al.. Astrometric and photometric characterization of  $\eta$  Tel B combining two decades of observations. *Astronomy & Astrophysics - A&A*, 2024, 687, <10.1051/0004-6361/202449222>. <insu-04836848>

**HAL Id: insu-04836848**

**<https://insu.hal.science/insu-04836848v1>**

Submitted on 13 Dec 2024

**HAL** is a multi-disciplinary open access archive for the deposit and dissemination of scientific research documents, whether they are published or not. The documents may come from teaching and research institutions in France or abroad, or from public or private research centers.

L'archive ouverte pluridisciplinaire **HAL**, est destinée au dépôt et à la diffusion de documents scientifiques de niveau recherche, publiés ou non, émanant des établissements d'enseignement et de recherche français ou étrangers, des laboratoires publics ou privés.



Distributed under a Creative Commons CC BY 4.0 - Attribution - International License

# Astrometric and photometric characterization of $\eta$ Tel B combining two decades of observations<sup>★</sup>

P. H. Nogueira<sup>1,2</sup>, C. Lazzoni<sup>3,2</sup>, A. Zurlo<sup>1,2</sup>, T. Bhowmik<sup>1,2</sup>, C. Donoso-Oliva<sup>4,2</sup>, S. Desidera<sup>5</sup>, J. Milli<sup>6</sup>, S. Pérez<sup>7,8,2</sup>, P. Delorme<sup>6</sup>, A. Fernandez<sup>4,2</sup>, M. Langlois<sup>5</sup>, S. Petrus<sup>1,2,7,8</sup>, G. Cabrera-Vives<sup>4,2,10</sup>, and G. Chauvin<sup>9</sup>

- <sup>1</sup> Instituto de Estudios Astrofísicos, Facultad de Ingeniería y Ciencias, Universidad Diego Portales, Av. Ejército 441, Santiago, Chile  
<sup>2</sup> Millennium Nucleus on Young Exoplanets and their Moons (YEMS), Chile  
e-mail: [nogueirapedro404@gmail.com](mailto:nogueirapedro404@gmail.com)  
<sup>3</sup> Department of Physics and Astronomy, University of Exeter, Stocker Road, Exeter EX4 4QL, UK  
<sup>4</sup> Department of Computer Science, Universidad de Concepción, Concepción 4070386, Chile  
<sup>5</sup> INAF-Osservatorio Astronomico di Padova, Vicolo dell'Osservatorio 5, 35122 Padova, Italy  
<sup>6</sup> Univ. Grenoble Alpes, CNRS, IPAG, 38000 Grenoble, France  
<sup>7</sup> Departamento de Física, Universidad de Santiago de Chile, Av. Victor Jara, 3659 Santiago, Chile  
<sup>8</sup> Center for Interdisciplinary Research in Astrophysics and Space Science (CIRAS), Universidad de Santiago de Chile, Santiago, Chile  
<sup>9</sup> Laboratoire Lagrange, UMR7293, Université Côte d'Azur, CNRS, Observatoire de la Côte d'Azur, Boulevard de l'Observatoire, 06304 Nice, France  
<sup>10</sup> Center for Data and Artificial Intelligence, Universidad de Concepción, Concepción, Chile

Received 12 January 2024 / Accepted 1 May 2024

## ABSTRACT

**Context.**  $\eta$  Tel is an 18 Myr system composed of a  $2.09 M_{\odot}$  A-type star with an M7-M8 brown dwarf companion,  $\eta$  Tel B. The two objects have a projected separation of  $4''.2$  ( $\sim 208$  au). This system has been targeted by high-contrast imaging campaigns for over 20 yr, facilitating its orbital and photometric characterization. The companion,  $\eta$  Tel B, both bright and on a wide orbit, is an ideal candidate for a detailed examination of its position and the characterization of its atmosphere.

**Aims.** To explore the orbital parameters of  $\eta$  Tel B, measure its contrast, and investigate its close surroundings, we analyzed three new SPHERE/IRDIS coronagraphic observations. Our objectives are to investigate the possibility of a circumplanetary disk or a close companion around  $\eta$  Tel B, and characterize its orbit by combining this new data set with archival data acquired in the past two decades.

**Methods.** The IRDIS data are reduced with state-of-the-art algorithms to achieve a contrast with respect to the star of  $1.0 \times 10^{-5}$  at the location of the companion. Using the NEGative Fake Companion technique (NEGFC), we measure the astrometric positions and flux of  $\eta$  Tel B for the three IRDIS epochs. Together with the measurements presented in the literature, the baseline of the astrometric follow-up is 19 yr.

**Results.** We calculate a contrast for the companion of 6.8 magnitudes in the  $H$  band. The separation and position angle measured are  $4''.218$  and  $167.3$  degrees, respectively. The astrometric positions of the companions are calculated with an uncertainty of 4 milliarcseconds (mas) in separation and 0.2 degrees in position angle. These are the smallest astrometrical uncertainties of  $\eta$  Tel B obtained so far. The orbital parameters are estimated using the Orvara code, including all available epochs. The orbital analysis is performed taking into account the *Gaia*-HIPPARCOS acceleration of the system. Suppressing its point spread function (PSF), we have produced contrast curves centered on the brown dwarf in order to constrain our detection capabilities for a disk or companions around it.

**Conclusions.** After considering only orbits that could not disrupt the outer debris disk around  $\eta$  Tel A, our orbital analysis reveals a low eccentric orbit ( $e \sim 0.34$ ) with an inclination of 81.9 degrees (nearly edge-on) and a semi-major axis of 218 au. Furthermore, we determine the mass of  $\eta$  Tel B to be  $48 M_{\text{Jup}}$ , consistent with previous calculations from the literature based on evolutionary models. Finally, we do not detect any significant residual pointing to the presence of a satellite or a disk around the brown dwarf. The retrieved detection limits allow us to discard massive objects around  $\eta$  Tel B with masses down to  $1.6 M_{\text{Jup}}$  at a separation of 33 au.

**Key words.** instrumentation: adaptive optics – methods: data analysis – techniques: high angular resolution – techniques: image processing – planets and satellites: detection – planet-disk interactions

## 1. Introduction

Since the first discovery of a planet around a main-sequence star (Mayor & Queloz 1995), techniques and instruments for discovering and characterizing substellar objects have advanced exponentially. Today, more than 5500 exoplanets have been

confirmed<sup>1</sup>, and more than 19 000 candidates of ultracool dwarfs (spectral type later than M7) are known (dal Ponte et al. 2023). However, little is known about where, when, and how substellar objects form. Thus, investigating newborn substellar objects in a stellar system is essential to address this knowledge gap, since

<sup>1</sup> Information extracted from the NASA Exoplanet archive database <https://exoplanetarchive.ipac.caltech.edu/> (Akeson et al. 2013).

<sup>★</sup> This publication made use of data from the ESO programs 095.C-0298(A), 097.C-0394(A), 198.C-0209(H), 1100.C-0481(G).

they are expected to retain signatures of their formation pathway through the system architecture (e.g., Mayer et al. 2004; Pearce & Wyatt 2014; Greaves et al. 2014; Davies 2019; Bowler et al. 2020; Do Ó et al. 2023) and from their atmosphere (e.g., Marley et al. 2007; Öberg et al. 2011; Dupuy et al. 2014; Baraffe et al. 2015; Crepp et al. 2018; Zhang et al. 2023; Petrus et al. 2024).

In particular, the high-contrast imaging technique (hereafter called HCI) is a capable tool to discover and characterize young giant planets and brown dwarfs. HCI is sensitive to recently formed objects that conserve some formation heat. Indeed, substellar objects have been discovered using HCI techniques in the past decade (e.g., 2MASSWJ 1207334-393254: Chauvin et al. 2004;  $\beta$  Pic b: Lagrange et al. 2010; HD 95086 b: Rameau et al. 2013a; PDS 70 b: Keppler et al. 2018; YSES 2b: Bohn et al. 2021). More recently, with the release of the *Gaia* catalogs and an update on astrometric precision, HCI has also been used to follow up on stars that showed anomalous accelerations (difference between their long-term HIPPARCOS-*Gaia* and short-term *Gaia* proper motion vectors), pointing towards the presence of companions in the system. One remarkable example is the discovery of AF Lep b through proper motion anomalies and HCI (Mesa et al. 2023; De Rosa et al. 2023; Franson et al. 2023).

Near-infrared substellar companions observed by HCI may offer valuable multiwavelength and multi-analysis data for the detection of circumplanetary disks (CPDs) or satellites in their surroundings. For instance, Pérez et al. (2019) analyzed ALMA band 6 observations featuring directly imaged companions, establishing upper limits on CPD detectabilities. Similarly, using SPHERE near-infrared (NIR) images, Lazzoni et al. (2020) set upper limits for satellite detections around substellar companions. Notably, Lazzoni et al. (2020) also identified a potential satellite candidate around DH Tau B, although confirmation of its nature is still pending. Subsequently, Lazzoni et al. (2022) provided a more robust analysis on the detectability of satellites through all standard exoplanet discovery techniques. Additionally, Ruffio et al. (2023) proposed to direct efforts towards detecting potential candidates through radial velocity monitoring, a method that can be implemented by monitoring companions with high-resolution spectroscopy. Another technique for searching for satellites is spectroastrometry, which consists of the fine measurement of any deviation from the position of the center of light (Agol et al. 2015). If an integral field spectrograph targets an unresolved planet-satellite system, it is expected that the center of the light shifts position depending on the wavelength. The movement of the centroid of the PSF would reveal if a satellite is present.

One system that comes to attention based on its age, being targetable from HCI and satellite analysis, and its astrometric follow-up is  $\eta$  Telescopii (hereafter called  $\eta$  Tel).  $\eta$  Tel is part of the  $\beta$  Pic moving group, with an estimated age of 18 Myr Miret-Roig et al. (2020) and a distance of 49.5 pc (Bailer-Jones et al. 2021). It is composed of an A0V, 2.09  $M_{\odot}$  primary star ( $\eta$  Tel A; Houk & Cowley 1975; Desidera et al. 2021a,b) and an M7-8, brown dwarf companion ( $\eta$  Tel B) at  $\sim 4''.2$  separation and position angle of  $\sim 169^{\circ}$  (Lowrance et al. 2000; Guenther et al. 2001, and references therein).  $\eta$  Tel A presents a likely warm debris belt at 4 au (unresolved, only inferred from the SED) and an edge-on cold debris belt at 24 au discovered via infrared excess (Backman & Paresce 1993; Mannings & Barlow 1998). The outer debris disk was later resolved with T-ReCS (Thermal-Region Camera Spectrograph) on Gemini South (Smith et al. 2009). Moreover, despite gas absorption towards

$\eta$  Tel debris disc was previously attributed to radiatively driven debris consistent with C/O solar ratio (Youngblood et al. 2021), more recent findings revealed that the origin of absorption lines is more likely of an interstellar cloud traversing the line of sight of  $\eta$  Tel A (Iglesias et al. 2023).  $\eta$  Tel B is a bright substellar companion with a contrast of 6.7 magnitudes in the VLT/NACO  $H$  band (Neuhäuser et al. 2011), or 11.85 in apparent magnitude. Its astrometrical points and orbital constraints were first compiled and analyzed in Neuhäuser et al. (2011), which used 11 yr of imaging data (1998–2009). An additional NACO observation was presented in Rameau et al. (2013b), which broadened the time baseline to 2011.

In this paper, we present a characterization of the companion, including astrometrical and photometrical follow-up and orbital constraint analysis. We present three new epochs from the Spectro-Polarimetric High-contrast Exoplanet REsearch (SPHERE) instrument (Beuzit et al. 2019). With the addition of the new SPHERE data and a baseline of observations from 1998 to 2017, we present the most recent and complete orbital characterization of the system. Furthermore, we performed an analysis of the surroundings of  $\eta$  Tel B to constrain the possible presence of features such as satellites or circumplanetary disks.

The manuscript is structured in the following order. Observations and data reduction are described in Sect. 2. The photometric and astrometric measurements of the system of the new SPHERE observations are reported in Sect. 3.1. The orbital fitting analysis, taking into account the new data and the literature can be found in Sect. 3.2. The description of the study of the close vicinity of the substellar companion and the contrast curves around  $\eta$  Tel B are presented in Sect. 4.3. Final remarks and conclusions are presented in Sect. 5.

## 2. Observations and data reduction

### 2.1. Observations

We present new SPHERE/IRDIS coronagraphic data of the system around  $\eta$  Tel A. SPHERE is a VLT (Very Large Telescope) planet-finder instrument located at Paranal, Chile – UT3. It is an instrument dedicated to HCI. SPHERE is composed of four main scientific parts: the Common Path and Infrastructure (CPI), which includes an extreme adaptive optics system (SAXO, Fusco et al. 2006; Petit et al. 2014) and coronagraph systems; the Infrared Dual-band Imager and Spectrograph (IRDIS, Dohlen et al. 2008) with a pixel scale of 12.25 mas and field of view (FoV) of  $11 \times 12.5$  arcsec; the integral field spectrograph (IFS, Claudi et al. 2008) with FoV of  $1''.73 \times 1''.73$ ; and the Zurich Imaging Polarimeter (ZIMPOL, Schmid et al. 2018), the visible light imager and polarimeter of SPHERE. Both IRDIS and IFS belong to the NIR branch and can be used concomitantly if required during observations. Given the separation of  $\eta$  Tel B and its brightness in the near-infrared, IRDIS observations are the most suitable for the purpose of our paper.

The observations were performed with IRDIS on three different nights. Since the stellar companion is outside the field of view (FoV) of the integral field spectrograph (IFS) instrument, we do not report its data in this manuscript. The first observation (program 095.C-0298(A); PI Beuzit) was taken on 2015-05-05, generally under average conditions, with variable seeing ranging between 1 and 2 arcsec (this epoch had photometric sky transparency). The second observation (program 097.C-0394(A); PI Milli) was taken under good conditions on 2016-06-15, and the seeing was mostly stable during the period

**Table 1.** List of the SPHERE/IRDIS  $\eta$  Telescopii observations used in this work.

Date (UT)	ESO ID – PI	IRDIS filter	DIT $\times$ NDIT	$\Delta$ PA	Seeing (")	Avg. coherence time (s)
2015-05-05	095.C-0298(A)- Beuzit	DB_H2H3	32 $\times$ 8	46.83	Mostly 0.9–1.5 <sup>(a)</sup>	0.0011
2016-06-15	097.C-0394(A)- Milli	BB_H	8 $\times$ 8	18.17	1–1.4	0.0024
2017-06-15	198.C-0209(H)- Beuzit	DB_H2H3	32 $\times$ 12	2.04	1.5–2	0.0023
2018-05-08 <sup>(b)</sup>	1100.C-0481(G)- Beuzit	–	–	–	–	–

**Notes.** <sup>(a)</sup>A subtle increase in seeing above 1.5 was registered between 08h40m–9h00m UTC at that night. <sup>(b)</sup>Discarded from the analysis for bad observing conditions.

of observation, varying between 1–1.4 arcsec (this epoch had the sky transparency declared as thin). This program was performed as part of the SPHERE High-Angular Resolution Debris Disks Survey (SHARDDS; [Dahlqvist et al. 2022](#)), designed to image circumstellar disks around bright nearby stars (within 100 pc from the Earth). The third observation (program 198.C-0209(H); PI Beuzit) was taken on 2017-06-15, with a slightly higher value of the seeing and poorer conditions (“thin” sky transparency). An apodized Lyot coronagraph (N\_ALC\_YJH\_S; inner working angle  $\sim 0''.15$ ) was used on all three nights. A dual-band filter H2H3 was set ( $\lambda = 1.593$  and  $1.667 \mu\text{m}$  for H2 and H3, respectively;  $\Delta\lambda = \sim 0.053 \mu\text{m}$  for both filters) on the first and third nights, while on the second night, a broadband filter H ( $\lambda = 1.625 \mu\text{m}$ ;  $\Delta\lambda = 0.29 \mu\text{m}$ ) was used instead. A fourth IRDIS sequence was taken (2018-05-08; ID: 1100.C-0481(G); PI: Beuzit), but it was discarded from our analysis due to bad observing conditions. The observations and their specifications are summarized in Table 1.

## 2.2. Data reduction

The reduction of the three epochs was performed by the High Contrast Data Center pipeline<sup>2</sup> (hereafter called as HC DC; [Delorme et al. 2017](#)), which utilizes the Data Reduction and Handling software (v0.15.0; [Pavlov et al. 2008](#)) and routines presented in [Galicher et al. \(2018\)](#). The process includes standard pre-reduction steps such as background subtraction, flat-fielding, and bad pixel correction. The frames are recentered using the SPHERE waffle pattern, followed by corrections for the anamorphism of the instrument and astrometric calibration (pixel scale and True north correction), as described in [Maire et al. \(2016\)](#). The final products comprise a master cube that contains all frames, the position angle (PA) values of each frame, and an off-axis PSF reference cube. The off-axis PSF is an unsaturated image of the central star taken before and after the coronagraphic sequence for flux calibration.

We made use of the VIP code (Vortex Image Processing, [Gomez Gonzalez et al. 2017](#); v.1.5.1) to reject the bad frames in each master cube, considering only frames with a Spearman correlation above 0.85 compared to the first frame taken under good conditions. After this step, we created post-processing images, employing the Angular Differential Imaging (ADI; [Marois et al. 2006](#)) and principal component analysis (PCA; [Soummer et al. 2012](#); [Amara & Quanz 2012](#)) with varied numbers of principal components. Since the PCA introduces deep over-subtraction due to the FoV rotation even for a few components, we favored the classical ADI images for our analysis. The result of this post-processing technique is presented in Fig. 1.

<sup>2</sup> Formerly known as SPHERE Data Center or SPHERE DC.

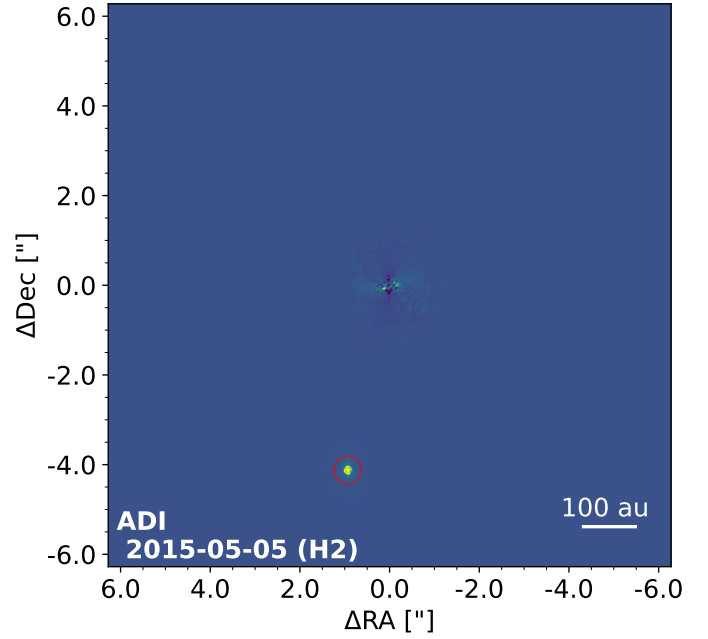


**Fig. 1.** ADI-processed from IRDIS coronagraphic sequence (epoch: 2015-05-05; filter: H2) for the  $\eta$  Tel system. The red circle marks the position of  $\eta$  Tel B. The star is masked under the coronagraph at the center of the image. North is up, East is left.

## 3. Methodology and results

### 3.1. Astrometry and photometry

#### 3.1.1. The NEGFC technique

To precisely determine the position and flux of  $\eta$  Tel B, we employed the NEGative Fake Companion Technique (NEGFC), as described in studies such as [Lagrange et al. \(2010\)](#) and [Zurlo et al. \(2014\)](#). This technique involves modeling the target source by introducing a negative model of the instrumental PSF into the pre-processed data. The procedure aims to minimize residuals in the final image, adjusting the flux and position of the model to align with the source’s properties (astrometry and photometry). We implemented the NEGFC using the VIP package.

For this purpose, we adapted the `single_framebyframe` routine proposed by [Lazzoni et al. \(2020\)](#). This routine provides estimates of separation, position angle, and photometry for the companion in each frame from the coronagraphic sequence.  $\eta$  Tel B’s brightness (signal-to-noise ratio  $\geq 100$ ) and relative distance from the speckle-dominated region are sufficient for this approach to be applicable.

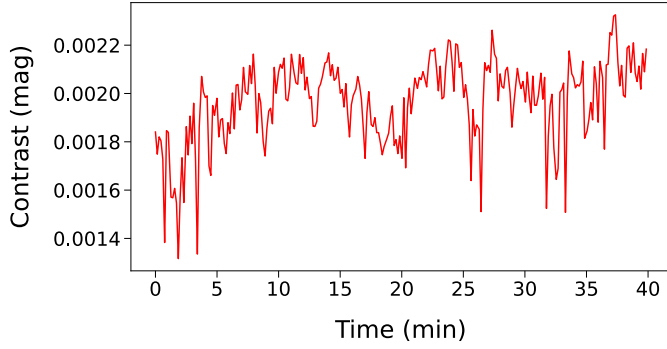


**Fig. 2.** Contrast flux variations for the companion with respect to the star (filter: BB\_H).

**Table 2.** IRDIS flux contrast in flux and magnitude with respect to the central star for  $\eta$  Tel B.

Epoch	Filter	Contrast [e-3]	$\Delta$ magnitude
2015-05-05	H2	$1.52 \pm 0.60$	$7.05 \pm 0.45$
2015-05-05	H3	$1.92 \pm 0.12$	$6.79 \pm 0.07$
2016-06-15	BB_H	$2.00 \pm 0.17$	$6.75 \pm 0.09$
2017-06-15	H2	$1.53 \pm 0.78$	$7.04 \pm 0.61$
2017-06-15	H3	$1.92 \pm 0.84$	$6.79 \pm 0.51$

As a model PSF, we utilized the off-axis image of the central star captured before and after the coronagraphic sequence. For each set of coordinates, a negative flux was introduced, and the set of positions and fluxes yielding the lowest residual (standard deviation) in each frame was selected. Consequently, for each night and filter, the routine's results were represented by the median values of the parameters measured across all frames.

### 3.1.2. Measurement of the photometry

The contrast of the brown dwarf was calculated as the median of the NEGFC technique values on each frame of the coronagraphic sequence. Flux contrast uncertainties were derived from the standard deviation of the fluxes measured by the NEGFC technique. Figure 2 sets flux measurements throughout the sequence using BB\_H filter, showing how the values can vary. The contrast in flux and magnitude with respect to the central star for each filter is shown in Table 2. The results are consistent with the measurements presented in the literature for the companion.

After using the NEGFC technique, the signal of the companion was removed in each frame of the datacubes, creating therefore empty datacubes. Following, a 5-sigma contrast curve with respect to and around  $\eta$  Tel A was produced using the ADI processed data. The achieved contrast for epoch 2016-06-15 is shown in Fig. 3.

### 3.1.3. Measurement of the astrometric positions

To robustly determine the separation and position angle at each epoch, we applied multiple methods while concurrently estimating the disparities between these algorithms. Specifically, we employed:

- the NEGFC method detailed in Sect. 3.1.1;

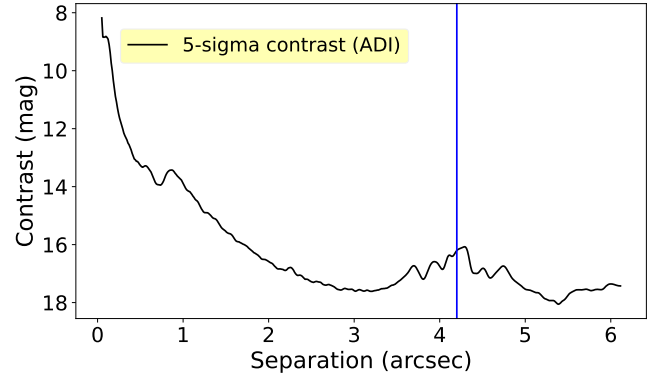


**Fig. 3.** Contrast curve with respect to  $\eta$  Tel A, using the datacube corresponding to the 2016-06-15 (BB\_H) observation. The vertical blue line corresponds to the position of the companion.

- a 2D-Gaussian fitting encompassing the companion. We optimized Gaussian statistics using two stochastic algorithms: Adam (Kingma & Ba 2014) and the Levenberg–Marquardt algorithm (Moré 2006);
- the peak intensity pixel location within a FWHM of the companion.

All the algorithms were applied to each frame of the coronagraphic (frame-by-frame) sequence as well as to their median-collapsed reduction. When using the frame-by-frame method, it is important to note that a sequence of positions is obtained and it is necessary to reduce them by using the median. Finally, the astrometric points for each night and filter were determined by calculating the median among the outputs of the algorithms. Similarly, the uncertainties of the astrometric fitting were calculated as the standard deviation across all results obtained from the various methods. We justify applying different methods as we observed that the final results of each method could differ by a maximum of 10 mas in separation and approximately 0.15 degrees in position angle. Therefore, we opted for implementing a median instead of an average to filter out values that may otherwise skew the results.

In addition to the uncertainties on the astrometric fitting of the companion, we have to consider other factors in the error budget, as previously stated by Wertz et al. (2017):

- Instrumental calibration, where the most relevant errors come from the orientation of the True North, pupil offset, plate-scale, and anamorphism;
- Determination of the position of the central star behind the coronagraph;
- Systematic error due to residual speckles;
- Statistical error due to planet position determination.

Therefore, considering  $R$  as the final expression for radial separation in arcseconds and  $\Theta$  as the final expression for position angle in degrees, we applied the following approximated equations:

$$R = PS(R_* \pm R_{\text{spec}} \pm rR_{\text{AF}} \pm r) \quad \text{and} \quad (1)$$

$$\Theta = \Theta_* \pm \Theta_{\text{spec}} \pm \Theta_{\text{AF}}\theta \pm \Theta_{\text{PO}} \pm \Theta_{\text{TN}} \pm \theta, \quad (2)$$

where  $r$  is the radial distance and  $\theta$  the position angle,  $R_*$  and  $\Theta_*$  the radial and azimuthal values related to stellar centering;  $R_{\text{spec}}$  and  $\Theta_{\text{spec}}$  the radial and azimuthal values related to speckle noise;  $R_{\text{AF}}$  and  $\Theta_{\text{AF}}$  values related to the anamorphic factor expressed in percentage; TN related to the true north, PS to

plate scale ("/pixel) and PO to the pupil offset. All distances are measured in pixels and all angles are measured in degrees.

Consequently, the Eqs. (1) and (2) can be used to propagate the errors:

$$\sigma_R^2 = PS^2[\sigma_{R_{\text{spec}}}^2 + \sigma_{R_s}^2 + r^2\sigma_{R_{\text{AF}}}^2 + (R_{\text{AF}} + 1)^2\sigma_r^2] + \frac{R^2}{PS^2}\sigma_{PS}^2 \quad (3)$$

and,

$$\sigma_\Theta^2 = \sigma_{\Theta_{\text{spec}}}^2 + \sigma_{\Theta_s}^2 + \theta^2\sigma_{\Theta_{\text{AF}}}^2 + \sigma_{\text{PO}}^2 + \sigma_{\text{TN}}^2 + (\Theta_{\text{AF}} + 1)^2\sigma_\theta^2. \quad (4)$$

The instrumental calibration uncertainties were determined through astrometric calibrations outlined in Maire et al. (2016, 2021), and the last version of the SPHERE manual, 18th release. Before July 2016, an issue with the synchronization between SPHERE and VLT internal clocks led to abnormal fluctuations in True North measurements. Consequently, for the initial two  $\eta$  Tel observations, the True North uncertainties were extracted from Table 3 of Maire et al. (2016). For the third observation, we adopted a fixed value of  $0.04^\circ$ , representing the stabilized uncertainty following calibrations and corrections.

The plate (pixel) scale uncertainties, were extracted from close-in-time coronagraphic observations, obtained with the SPHERE-SHINE GTO data, using the globular stellar cluster 47 Tuc as field reference (Table 7 of Maire et al. 2021). The pupil offset uncertainty, derived from commissioning and guaranteed time observations, is 0.11 degrees. Distortion is predominantly influenced by a  $0.60\% \pm 0.02\%$  anamorphism between the horizontal and vertical axes of the detector. Since each frame has undergone correction by the HC DC, rescaling each image by 1.006 along the axis, the uncertainty of 0.02% (for both  $R_{\text{AF}}$  and  $\Theta_{\text{AF}}$ ) was incorporated into the error budget analysis.

The radial stellar centering uncertainty per dithering is 1.2 mas, derived from observations of bright stars during commissioning runs (Zurlo et al. 2014, 2016). This value was then adjusted by dividing it by the square root of the number of frames per observation. Subsequently, the latter was translated into an uncertainty on position angle by division by the separation  $r$  of the companion.

Uncertainties arising from speckles may persist even after ADI post-processing and have an impact on photometric and astrometric measurements (Guyon et al. 2012; Wertz et al. 2017). To address this, we employed the `speckle_noise_uncertainty` function from VIP, injecting multiple simulated companions into companion-free cubes at the same radial distance and flux as the actual companion. The positions of these simulated companions were determined using Nelder–Mead optimization, and then the values of separation and position angle were measured. By comparing the offsets between the input values and the estimations by the code, a distribution of parameters was generated. A Gaussian function was then fitted to the distribution, and the uncertainties in  $R$  and  $\Theta$  were estimated as the standard deviations of the fitting. In this instance, a total of 100 simulated companions, equally spaced azimuthally, were utilized. A similar methodology was employed by Maire et al. (2015); Wertz et al. (2017). In Fig. 4, three histograms illustrate the distribution of separation, position angle, and flux of the companion observed on 2015-05-05. The separation and position angle values for the epoch are shown in Table 3, and the detailed uncertainties used to calculate the error budget are compiled in Table 4.

**Table 3.** List of astrometric positions of  $\eta$  Tel B obtained from the IRDIS observations.

Epoch	Filter <sup>(a)</sup>	Sep. (")	PA (°)
2015-05-05	H3	$4.215 \pm 0.004$	$167.326 \pm 0.197$
2016-06-15	BB_H	$4.218 \pm 0.004$	$167.260 \pm 0.130$
2017-06-15	H2	$4.218 \pm 0.004$	$167.346 \pm 0.142$

**Notes.** The error budget is listed in Table 4. <sup>(a)</sup>The table only presents values related to the filters where the lowest uncertainties, retrieved from NEGFC, on each epoch, were achieved.

### 3.2. Orbital fitting analysis

The system around  $\eta$  Tel A was observed with the high-contrast imaging technique for the last two decades. The favorable contrast of the brown dwarf companion and the wide separation between the two objects make the system an ideal target for HCI. The astrometric follow-up of the brown dwarf companion counts 18 epochs of observation spanning almost 20 yr. For the orbit analysis, we included all the astrometrical points presented in the literature, as well as the ones obtained from the new analysis. The complete list is shown in Table 5 and their positions with respect to the central star are represented in Fig. 5.

We employed the Orvara code (Orbits from Radial Velocity, Absolute, and/or Relative Astrometry; Brandt et al. 2021) to perform the orbital fitting of the system. Orvara accepts input information on the acceleration of the central star from the Hipparcos vs. *Gaia* early data-release 3 (EDR3; Bailer-Jones et al. 2021) catalogs.

The orbital elements and masses of both the host and the companion were computed by Orvara using a parallel tempered Markov chain Monte Carlo (MCMC) ensemble sampler, `ptemcee` (Voussen et al. 2016), a variant of `emcee` (Foreman-Mackey et al. 2013). Parallel tempering enhances the exploration of complex parameter spaces by simultaneously running multiple chains at different temperatures, allowing for more efficient sampling and improved convergence compared to traditional MCMC methods. In a simulation, different temperatures refer to variations in the parameter that control the acceptance of proposed moves in the MCMC algorithm. Higher temperatures encourage more exploration by accepting moves that might increase energy or objective function values, allowing the algorithm to escape local optima and explore a broader solution space. On the other hand, lower temperatures favor exploitation, focusing on refining solutions and improving the chance of finding the global optimum. Adjusting temperatures during the simulation influences the balance between exploration and exploitation, shaping the algorithm's behavior throughout the MCMC process. The MCMC simulation utilized 10 temperatures, 500 walkers, and  $10^6$  steps for each chain. The simulation outputs a point every 1000 steps.

Priors for the MCMC include distributions of the masses of celestial objects, parallax, and proper motion of the system. Additionally, the initial orbital elements distribution for the companions (semi-major axis:  $a$ ; eccentricity:  $e$ ; argument of the pericenter:  $\omega$ ; inclination:  $i$ ; longitude of the ascending node:  $\Omega$ ; and longitude at reference epoch:  $l$ ) can also be incorporated. We used as priors the common proper motion extracted from Kervella et al. (2021, 2022), the parallax from *Gaia* DR3 (Bailer-Jones et al. 2021), the primary mass from

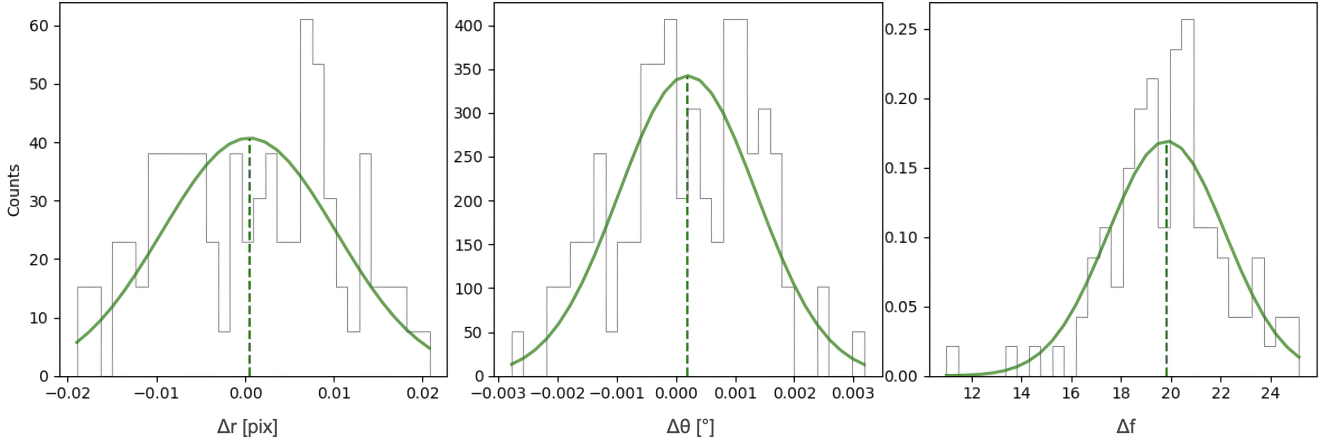


**Fig. 4.** Speckle noise estimation for  $\eta$  Tel B in the data set of 2015-05-05. The histograms illustrate the offsets between the true position and flux of a fake companion and its position and flux obtained from the NEGFC technique. The dashed lines correspond to the 1D Gaussian fit from which we determined the speckle noise.

**Table 4.** Uncertainties used to calculate the error budget for the astrometry of the companion.

Epoch	$\sigma_r$ (pixels)	$\sigma_{R_{\text{spec}}}$ (pixels)	$\sigma_{R_*}$ (pixels)	$\sigma_{R_{\text{AF}}}$ (%)	$\sigma_{PS}$ (mas pixel <sup>-1</sup> )	$\sigma_\theta$ (°)	$\sigma_{\Theta_{\text{spec}}}$ (°)	$\sigma_{\Theta_*}$ (°)	$\sigma_{\Theta_{\text{AF}}}$ (%)	$\sigma_{\text{PO}}$ (°)	$\sigma_{\text{TN}}$ (°)
2015-05-05	0.297	0.003	0.098	0.02	0.01	0.068	0.0005	0.016	0.02	0.11	0.145
2016-06-15	0.065	0.001	0.098	0.02	0.01	0.012	0.0001	0.016	0.02	0.11	0.060
2017-06-15	0.245	0.010	0.098	0.02	0.01	0.072	0.0015	0.016	0.02	0.11	0.040

**Notes.** The values correspond to errors associated with individual frames. The table only presents values related to the filters where the lowest uncertainties on each epoch were achieved: 2015-05-05 (H3); 2016-06-15 (BB\_H), and 2017-06-15 (H2), thus referring to the filters also listed on Table 3.

Desidera et al. (2021a,b), and the companion ( $\eta$  Tel B) mass with loosened constraints on its uncertainties from Lazzoni et al. (2020). Given the low orbital coverage from relative astrometric points, we just set a mean initial value inspired by the semi-major axis proposed by (Neuhäuser et al. 2011), leaving other orbital elements to cover wider values in the parameter space, as set by standard values from ORVARA. The specific priors and initial values set are detailed in Table 6. Further orbital constraints and results are analyzed and presented in Sect. 4.1.

## 4. Discussion

### 4.1. Orbital fitting constraints

From the results of the MCMC simulation, we excluded the orbits that may cause instability in the system. In order to prevent disruption of the debris disk by the close-by passage of  $\eta$  Tel B, and considering that the masses of the star and companion are well-constrained by the MCMC simulations, we can delimit the possible orbits for  $\eta$  Tel B by inspecting the brown dwarf-disk interaction. Before applying any constraint, we obtained as values the mass of  $\eta$  Tel A ( $m_* = 2.09 M_\odot$ ) and mass of  $\eta$  Tel B ( $m_{\text{comp}} = 48.10 M_{\text{Jup}}$ ) from the original ORVARA simulation.

In this context, it is useful to introduce the concept of chaotic zone, a region in the proximity of the orbit of a planet or brown dwarf which is devoid of dust grains, since its gravitational influence sweeps out small dust particles. The chaotic zone depends on the ratio between the mass of the brown dwarf and

the mass of the star, on the semi-major axis and eccentricity of the orbit. Given the outer disk's position, it is established that this zone cannot extend below 24 au. As  $\eta$  Tel B is positioned outside the disk, we employed the procedure outlined in Lazzoni et al. (2018) to compute the chaotic zone's extension for each orbit during the pericenter passage. Specifically, we utilized equation 10 for cases where the eccentricity is less than a critical value ( $e_{\text{crit}}$ ), or equation 12 for cases where it exceeds  $e_{\text{crit}}$ . Here,  $e_{\text{crit}}$  is determined as  $0.21\mu^{3/7}$ , equivalent to 0.022 ( $\mu$  is the ratio between the mass of the companion and the mass of the star). In the end, we discarded 326 674 orbits from an original number of 500 000.

Furthermore, another constraint arises when determining that the pericenter of the brown dwarf (BD) cannot reach the disk. Consequently, considering the semi-major axis of the companion established by the MCMC simulations, ( $a_{bd}^1 = 178$  au), we can use the following expression to discard highly eccentric orbits:

$$a_{bd}(1 - e_{\text{max}}) > 24 \text{ au} \quad (5)$$

where  $e_{\text{max}}$  is the maximum eccentricity allowed for the BD. Consequently, we obtained a maximum eccentricity of 0.865 and, therefore, we discarded an additional 139 orbits.

<sup>1</sup> The value of the semi-major axis of 178 au was the one retrieved before the exclusion of orbits. The final value is 218 au, as presented in Table 7 and Fig. A.1.

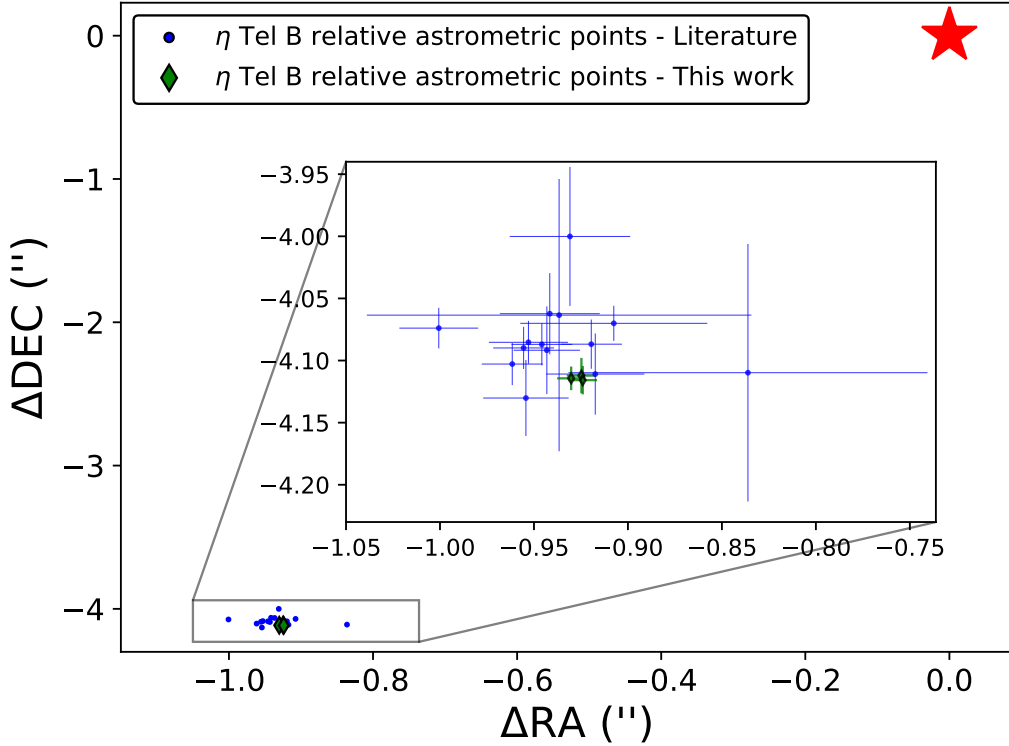


**Fig. 5.** Relative astrometry for  $\eta$  Tel B. The red star marks the position of  $\eta$  Tel A. The blue-filled circles represent astrometric points extracted from the literature. The green-filled diamonds represent the astrometric points from this work. The astrometric point from epoch 2000.378 was not included due to its high uncertainties.

**Table 5.** Astrometric positions of  $\eta$  Tel B from the literature and our analysis included in the Orvara analysis.

Date (yr)	Separation (")	PA ( $^\circ$ )	Ref.
1998.492	$4.170 \pm 0.033$	$166.95 \pm 0.36$	N11
2000.307	$4.107 \pm 0.057$	$166.90 \pm 0.42$	N11
2000.378	$4.310 \pm 0.270$	$165.80 \pm 6.70$	G01
2004.329	$4.189 \pm 0.020$	$167.32 \pm 0.22$	N11
2004.329	$4.200 \pm 0.017$	$166.85 \pm 0.22$	N11
2004.329	$4.199 \pm 0.036$	$167.02 \pm 0.22$	N11
2004.329	$4.195 \pm 0.017$	$166.97 \pm 0.22$	N11
2006.431	$4.170 \pm 0.110$	$167.02 \pm 1.40$	G08
2007.753	$4.212 \pm 0.033$	$167.42 \pm 0.35$	N11
2008.312	$4.214 \pm 0.017$	$166.81 \pm 0.22$	N11
2008.599	$4.195 \pm 0.017$	$166.87 \pm 0.29$	N11
2008.599	$4.194 \pm 0.016$	$166.20 \pm 0.29$	N11
2009.351	$4.239 \pm 0.104$	$168.50 \pm 1.30$	N11
2009.496	$4.199 \pm 0.031$	$166.99 \pm 0.30$	N11
2011.576	$4.170 \pm 0.009$	$167.43 \pm 0.70$	R13
2015.341	$4.215 \pm 0.004$	$167.33 \pm 0.20$	<sup>(a)</sup>
2016.454	$4.218 \pm 0.004$	$167.26 \pm 0.13$	<sup>(a)</sup>
2017.452	$4.218 \pm 0.004$	$167.35 \pm 0.14$	<sup>(a)</sup>

**References.** N11: Neuhäuser et al. (2011); G01: Guenther et al. (2001); G08: Geißler et al. (2008); R13: Rameau et al. (2013b); <sup>(a)</sup> this work.

Another constraint can be applied if we consider that the  $\eta$  Tel system has a wide comoving object, as mentioned previously in Neuhäuser et al. (2011). HD 181327 is an F5.5 V star, also a bona-fide member of the  $\beta$  Pic moving group, at a separation of  $\sim 7$  arcmin (20 066 au) (Holmberg et al. 2009; Neuhäuser et al. 2011; Bailer-Jones et al. 2021). The small proper motion

**Table 6.** Priors and initial and distribution of parameters for  $\eta$  Tel system astrometrical fitting<sup>(a)</sup>.

Priors	$\eta$ Tel A	$\eta$ Tel B
Mass ( $M_\odot$ )	$2.09 \pm 0.03$	$0.045 \pm 0.014$
Parallax (mas)	$20.603 \pm 0.099$	$20.603 \pm 0.099$
RA p.m. (mas/yr <sup>-1</sup> )	$25.689 \pm 0.006$	$25.689 \pm 0.006$
DEC p.m. (mas/yr <sup>-1</sup> )	$-82.807 \pm 0.006$	$-82.807 \pm 0.006$
Initial distribution <sup>(b)</sup>		
$a$ (au)	–	$220^{+300}_{-220}$
$\sqrt{e} * \sin(\omega)$	–	$0.4 \pm 0.3$
$\sqrt{e} * \cos(\omega)$	–	$0.4 \pm 0.3$
$i$ (radians)	–	$1.57 \pm 1.57$
$\Omega$ (radians)	–	$3.2 \pm 2.2$
$l$ (radians)	–	$0.8 \pm 0.5$

**Notes.** <sup>(a)</sup>Unphysical values such as negative values for masses or semi-major axis are automatically excluded from the code. <sup>(b)</sup>The initial distributions involve a lognormal distribution for the semi-major axis, while all other orbital values follow a normal distribution.

difference in *Gaia* DR3, corresponding to a velocity difference on the plane of the sky of 370 m/s, is compatible with a bound object. The nominal RV difference derived in Bailer-Jones et al. 2021; Zúñiga-Fernández et al. 2021, is instead larger than the maximum expected one for a bound object ( $\sim 400$  m/s). However, it is well possible that the published RV errors are underestimated for a star with an extremely fast  $v \sin i$  such as  $\eta$  Tel. There could also be contributions by additional objects, although both the *Gaia* RUWE (*Gaia* Renormalized Unit Weight Error) and the analysis of homogeneous RV time series do not indicate the presence of close companions (Lagrange et al. 2009; Grandjean et al. 2020). Therefore, we consider plausible, although not fully confirmed, that HD 181327 is bound to the  $\eta$  Tel system.

**Table 7.** Best orbital-fitting parameters for  $\eta$  Tel B calculated from the Orvara orbital characterization.

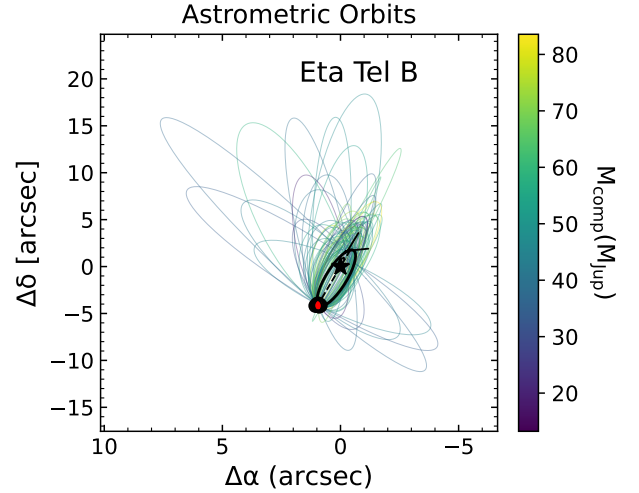
Mass ( $M_{\text{Jup}}$ )	$48^{+15}_{-15}$
$a$ (au)	$218^{+180}_{-41}$
$i$ (deg)	$81.9^{+3.2}_{-3.5}$
$\Omega$ (deg)	$174.6^{+175}_{-7.1}$
Mean longitude (deg)	$184^{+164}_{-74}$
Parallax (mas)	$20.60^{+0.10}_{-0.10}$
Period (yr)	$2201^{+3224}_{-592}$
$\omega$ (deg)	$159^{+128}_{-99}$
$e$	$0.34^{+0.26}_{-0.23}$
$a$ (mas)	$4486^{+3704}_{-845}$
Reference epoch $T_0$ (JD)	$2740996^{+488958}_{-107450}$
Mass ratio	$0.0219^{+0.0069}_{-0.0068}$

To ensure that HD 181327's presence in the system would not affect the long-term stability of  $\eta$  Tel B, we implemented Eq. 1 of (Holman & Wiegert 1999). Therefore, we could exclude orbits where the critical semi-major axis is greater than the periastron of the brown dwarf. To proceed, we used the mass of the perturber as  $1.3 M_{\odot}$  (Desidera et al. 2021a,b). Considering the eccentricities of the binaries as 0, a perturber with a similar mass would only impose constraints with a separation less than  $13''.25$  (656 au) from  $\eta$  Tel A. Otherwise, for HD 181327 to act as a perturber at its separation from the  $\eta$  Tel system, the eccentricities between HD 181327 and  $\eta$  Tel should be greater than 0.947. Therefore, we choose not to exclude any orbit using the external perturber criteria.

Following, the results of the simulation after the cut-off are shown as the corner plot in Fig. A.1 and also summarized in Table 7. The values obtained depict a pericenter of  $2''.9$  (144 au) and an apocenter of  $5''.9$  (292 au). Despite two decades of observations of  $\eta$  Tel B, the coverage only spans a fraction of the wide orbit of the companion, with a total  $\Delta\text{PA}$  of approximately  $\sim 2^\circ$ . This accounts for less than 1% of the orbit, assuming a face-on and circular orbit. Consequently, constraining the semi-major axis and eccentricity proves challenging. Nevertheless, the MCMC effectively determines the inclination, yielding an orbit that is nearly edge-on and almost co-planar with the debris disk (Smith et al. 2009). Conversely, a variety of possible orbits can adequately fit the data, as illustrated in Fig. 6.

#### 4.2. Possible formation scenarios

The coplanarity between  $\eta$  Tel B and the debris disk, as described in this work, and the relative spin-alignment between the star and the debris disk (Hurt & MacGregor 2023), can offer insights into the formation scenario of the system. Stellar systems form through various mechanisms, typically categorized into three main types: 1) fragmentation of a core or filament, 2) fragmentation of a massive disk, or 3) capture and/or dynamical interactions (for a comprehensive review, including separation and formation time scales, see Offner et al. 2023). Given the separation of the star and the companion, scenarios involving massive disk fragmentation or capture and/or ejection of  $\eta$  Tel B appear more plausible.


**Fig. 6.** 87 randomly selected possible orbits calculated by the Orvara fitting, after excluding orbits based on constraints described in Sect. 4.1. The black star indicates the position of  $\eta$  Tel A. The best-fit orbit is shown in black.

Alternatively, core fragmentation, which occurs through direct/turbulent fragmentation (e.g., Boss & Bodenheimer 1979; Bate & Burkert 1997) or rotational fragmentation (e.g., Larson 1972; Bonnell 1994; Bonnell & Bate 1994a,b; Burkert et al. 1997), followed by inward migration, is also a conceivable formation scenario. Binaries formed through direct fragmentation, with well-separated cores, may exhibit uncorrelated angular momenta between the objects (Offner et al. 2016; Bate 2018; Lee et al. 2019; Bate 2000). In contrast, stars and substellar objects formed through rotational fragmentation within the same plane tend to display preferentially spin-aligned and coplanar systems (Offner et al. 2016; Bate 2018). In such a case, a rotational fragmentation followed by inward migration becomes more probable.

Moreover, the eccentricity of the system plays a crucial role in inferring the formation scenario. If we consider the orbital fitting results where highly eccentric orbits are permitted, the preferred hypothesis for eccentricity enhancement would be recent dynamical interactions. If so,  $\eta$  Tel B did not reach near the debris disk of the star in the last few pericenter approximations. This scenario is highly improbable, given the short best-fitting orbital period in such cases ( $\sim 1623$  yr). It is more likely that  $\eta$  Tel B has a low eccentric orbit, and the assumptions for excluding highly eccentric orbits may be the most suitable approach. Consequently, the system exhibits quasi-coplanarity and low eccentricity of the companion. Therefore, we tentatively suggest that the preferred formation scenarios for  $\eta$  Tel involve either the fragmentation of a massive disk with slow or no inwards migration or rotational fragmentation of a core with fast inwards migration. Long-term RV and astrometry monitoring of the star and the companion, along with multiwavelength observations of the system, could be useful to discard a capture or ejection scenario.

#### 4.3. The close surroundings of $\eta$ Tel B

In our Solar System, planets and small-sized bodies are often surrounded by satellites and dust rings or disk-like features (see e.g. Alibert et al. 2005). For instance, there are approximately 200 natural satellites in the Solar System, most of

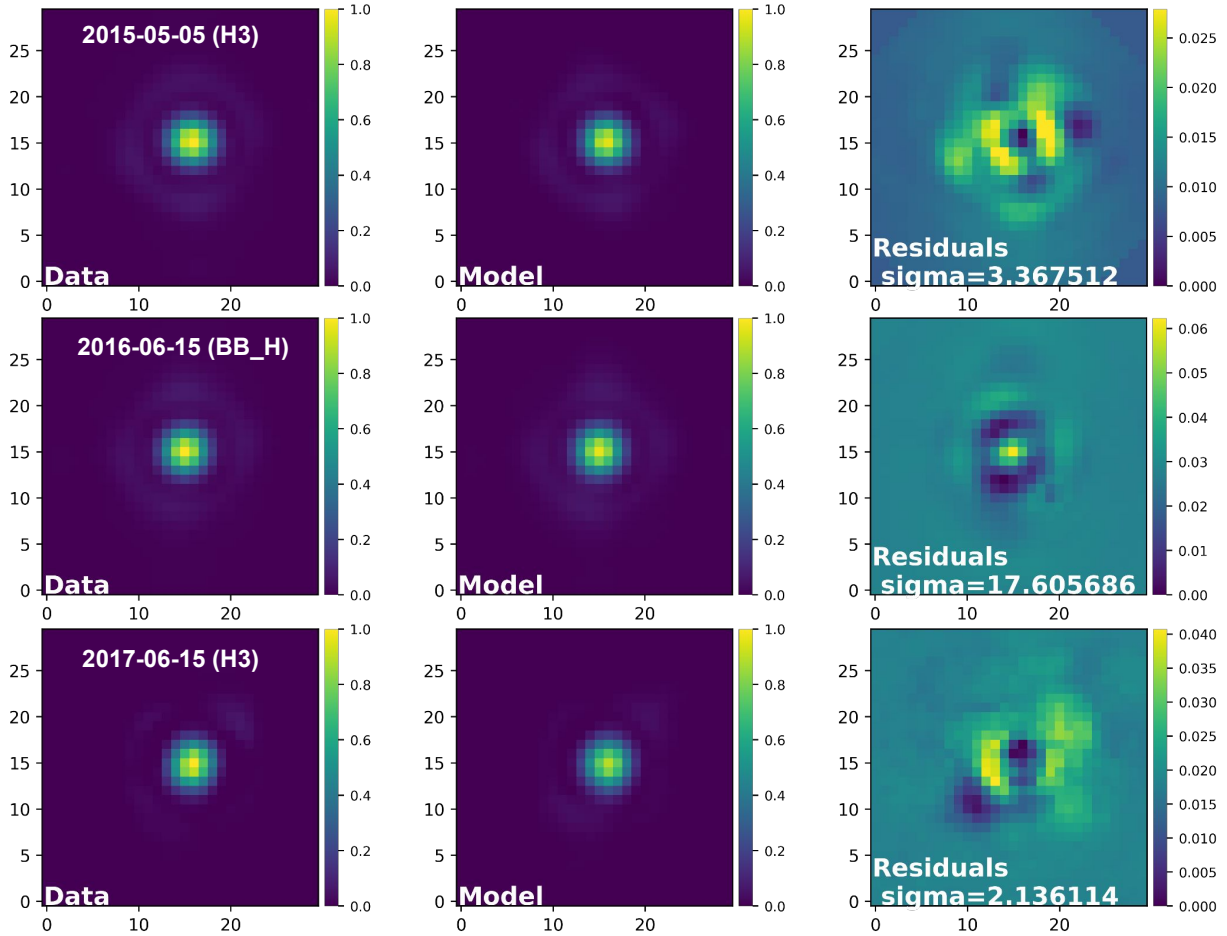


**Fig. 7.** Analysis of the close surroundings of  $\eta$  Tel B to look for satellites and/or CPDs. In each row, the first panel shows the ADI image zoomed on  $\eta$  Tel B, the second panel shows the model, and the last one the residuals from the subtraction of the two. The three IRDIS epochs are shown. The residuals are expressed in counts. All the panels were normalized to the peak of the central PSF.

which orbit giant planets. This raises the possibility of similar objects existing around substellar companions, although such discoveries have not yet been confirmed. Satellites or circumplanetary disks in these environments, if discovered, could provide valuable insights into their formation mechanisms. These mechanisms may include gravitational instability (Boss 1997 and references therein), core-accretion (Pollack et al. 1996 and references therein), or capture and/or orbital crossing, which can lead to satellite companions with specific mass ratios and orbits. For instance, less massive exomoons are likely to form within a circumplanetary disk (CPD), as observed with the Galilean moons (see, e.g., Canup & Ward 2002). Conversely, massive companion+satellite candidate systems likely form via orbital crossing+capture (Ochiai et al. 2014; Lazzoni et al. 2024). Furthermore, hydrodynamical simulations have shown that CPDs in the core-accretion scenario are eight times less massive and one order of magnitude hotter than those formed by gravitational instability (Szulágyi et al. 2017). Consequently, the characterization of exosatellites can be used to distinguish between these formation scenarios.

To analyze whether a satellite candidate or a CPD is present around the companion, we proceeded as follows: to compensate for the self-subtraction effect induced by post-processing, we forward-modeled the companion per frame based on the observations and the PSF model. With the pre-processed data,

the radial distance, position angle, and flux were obtained from the NEGFC approach (refer to Sect. 3.1.1). The off-axis PSF extracted before the sequence was positioned and flux-normalized with these parameters in an empty frame, creating what we refer to as “model”. Following, for each frame, the model was subtracted from the data, producing a residual image. The model and residual cubes were then collapsed using ADI or PCA+ADI. We compare the ADI post-processed data with the collapsed model and residual cubes per night in Fig. 7). The quality of the residuals is strongly related to the number of frames and quality of the night, showing a clearer result for the epoch 2016-06-15, where other epochs are more affected by systematics. Still, the residuals do not show any clear signal of a satellite or other nearby structure, imposing a threshold of detections at the contrast obtained with the NEGFC technique.

To generate contrast curves around  $\eta$  Tel B, we implemented a methodology similar to the one outlined in Lazzoni et al. (2020). The steps can be summarized as follows. Successive annuli, each centered on  $\eta$  Tel B and with a width equal to 1 FWHM, were chosen up to the Hill radius of the brown dwarf. The contrast at each radial position is computed as five times the standard deviation inside the annulus divided by the peak of the star ( $\eta$  Tel A).

For each annulus, we injected fake companions at various position angles, and their fluxes were determined after applying

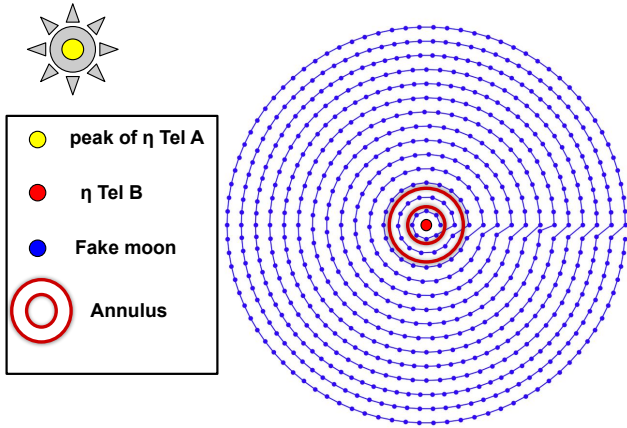


**Fig. 8.** Schematic representation of the placement of putative fake satellites around  $\eta$  Tel B to calculate the contrast curves. In this illustration, just one annulus is represented.

the NEGFC and PCA post-processing techniques. The ratio between the retrieved and injected flux provides the throughput value. A mean throughput is then calculated for each annulus and multiplied by the contrast at each separation. As a final step, we adjusted the contrast for small sample statistics, following the discussion presented in Mawet et al. (2014). A schematic representation of the steps used to calculate the contrast curves is illustrated in Fig. 8.

Finally, the contrasts were converted into mass constraints using the ATMO 2020 evolutionary models (Phillips et al. 2020). We utilized an estimated age for the system of 18 Myr (Miret-Roig et al. 2020) and a distance of 49.5 pc (Bailer-Jones et al. 2021). The best contrast curves for each data set are depicted in Fig. 9. We can discard the detection of satellites around the brown dwarf with masses between 3 and  $1.6 M_{\text{Jup}}$  in the range of distances [10, 33] au. Such massive objects, if present, would likely be the result of capture or trapping through tidal interactions (Lazzoni et al. 2024) or formation in situ via gravitational instability or direct collapsing. However, we cannot exclude the presence of closer-in and/or less massive objects which, for example, could have formed within a CPD via core accretion. Moreover, we can exclude the presence of an extended CPD from the shape and luminosity of the residuals around the companion.

## 5. Conclusions

In this paper, we present the most recent photometric and astrometric characterization of  $\eta$  Tel B, a brown dwarf situated at an approximate separation of  $\sim 4''.2$  from its host star. The observations of this system were conducted using SPHERE/IRDIS H2H3 and BB\_H filters, spanning three epochs across three consecutive years (2015–2017).

To robustly establish astrometry and photometry for the sub-stellar companion, we employed the NEGFC customized routine presented in Lazzoni et al. (2020). This approach was applied to each frame of the scientific datacube, as opposed to solely in the post-processed ADI image, as is conventionally practiced. Photometric results were derived by considering the median of each set of parameters per observation. Photometric errors were determined based on the standard deviation of the fluxes obtained per night. Astrometrical results (separation of  $4.218 \pm 0.004$  arcsecs and position angle of  $167.3 \pm 0.2$  degrees) were made taking into account not only the NEGFC approach

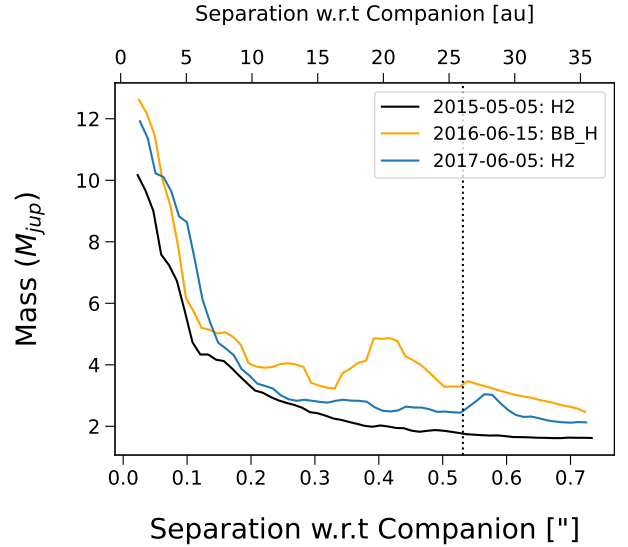


**Fig. 9.** Contrast curves with respect to the star  $\eta$  Tel A, centered on the companion as depicted in Fig. 8. The three contrast curves, corresponding to different epochs, are showcased. The vertical dashed line indicates the Hill radius of  $\eta$  Tel B under the assumption of an orbit with an eccentricity of  $e=0.34$ .

but also incorporated an analysis using 2D Gaussian fitting and position of the peak intensity of the companion. This analysis was made for both the frame-by-frame approach and the median-collapsed ADI image. The final values represent the median of each approach. In addition, for the uncertainties, systematic and statistical uncertainties, akin to the methodology employed by Wertz et al. (2017), were employed. The separation reached depicts a 4–70 times improvement in precision in comparison with previous NACO observations described and observed by Neuhäuser et al. (2011), and  $\sim 2$  times better precision than the L' NACO observations from Rameau et al. (2013b).

Furthermore, we conducted a comprehensive orbital characterization by compiling previous astrometric data, the new SPHERE data, and the HIPPARCOS-*Gaia* acceleration catalog, resulting in an orbital coverage spanning approximately 19 yr. The findings indicate a well-characterized companion mass of  $48 \pm 15 M_{\text{Jup}}$ , with the best-fitting orbit demonstrating near-edge-on orientation ( $i = 81.9$  degrees) and low eccentricity ( $e = 0.34$ ) when excluding orbits that can disrupt the debris disk around the star. However, it is essential to note that our observations did not encompass a significant portion of the entire orbit, leading to elevated uncertainties regarding the companion's orbital shape, period, eccentricity, and semi-major axis. We also highlight that due to the low orbital coverage, the orbital fitting presented represents a plausible family of orbits, and the orbital values listed in Table 7 must be taken as an example of a possible orbit. Further follow-ups will better constrain the orbit of the BD in the future. Also, based on the high  $v \sin i$  of  $\eta$  Tel A, and the possible uncertainties on its measurements, we consider it plausible that HD 181327, at a separation of 20 066 au, is bound to the system.

A brief discussion about possible formation scenarios has been conducted. The coplanarity between  $\eta$  Tel B and its debris disk, along with the relative spin alignment between the star and the debris disk, provides valuable insights into the system's formation. Stellar system formation scenarios were categorized into three main types: fragmentation of a core or filament, fragmentation of a massive disk, or dynamical interactions. Based on the separation of the star and companion, the likelihood of

massive disk fragmentation or capture or ejection of  $\eta$  Tel B was highlighted as more plausible. Alternatively, the system's low eccentricity also allows for rotational fragmentation from a core scenario, if followed by fast inward migration. In summary, we tentatively propose the preferred formation involves either massive disk fragmentation with slow or no inward migration or rotational fragmentation of a core with faster inward migration, whereas continuous monitoring and multiwavelength observations are crucial for refining these conclusions and further understanding the system's dynamics.

Lastly, a meticulous analysis of the companion's surroundings was undertaken by subtracting the companion's signal using instrument-response models. No clear signal of a substructure or satellite was seen. We conclude the systematics heavily affected the residuals. From the contrast curves generated in the regions surrounding the companion, we can discard satellites down to 3 and 1.6  $M_{\text{Jup}}$  in the range of distances [10, 33] au, setting an upper limit on gravitational instability binary pairs or massive objects captured through tidal interactions at wider separations.

Future observations of the system with the next generation of high-contrast imagers mounted on space telescopes, likewise, JWST (*James Webb Space Telescope*) will further constrain the orbital analysis of the brown dwarf companion and allow for deeper contrast around the central star and the companion. This advancement will enable deeper contrast observations around both the central star and its companion. In the specific case of RV monitoring for detecting objects at closer separations, instruments like CRIFES+ (Cryogenic high-resolution InfraRed Echelle Spectrograph) or HiRISE (High Resolution Imaging Science Experiment), are suitable. Possible additional companions to the central star or the brown dwarf may be detected in the future.

*Acknowledgements.* The authors thank the anonymous referee for the fruitful comments and suggestions. The authors acknowledge support from ANID – Millennium Science Initiative Program – Center Code NCN2021\_080. P.H.N. acknowledges support from the ANID Doctorado Nacional grant 21221084 from the government of Chile. T.B. acknowledges financial support from the FONDECYT postdoctorado project number 3230470. SD acknowledges support by the PRIN-INAF 2019 “Planetary systems at young ages (PLATEA)”. S.P. acknowledges support from FONDECYT Regular grant 1231663. G.C.V. acknowledges support from FONDECYT Regular grant 1231877. This work has made use of the High Contrast Data Centre, jointly operated by OSUG/IPAG (Grenoble), PYTHEAS/LAM/CeSAM (Marseille), OCA/Lagrange (Nice), Observatoire de Paris/LESIA (Paris), and Observatoire de Lyon/CRAL, and supported by a grant from Labex OSUG@2020 (Investissements d’avenir – ANR10 LABX56).

## References

- Agol, E., Jansen, T., Lacy, B., Robinson, T. D., & Meadows, V. 2015, *ApJ*, **812**, 5
- Akeson, R. L., Chen, X., Ciardi, D., et al. 2013, *PASP*, **125**, 989
- Alibert, Y., Mousis, O., & Benz, W. 2005, *A&A*, **439**, 1205
- Amara, A., & Quanz, S. P. 2012, *MNRAS*, **427**, 948
- Backman, D. E., & Paresce, F. 1993, in *Protostars and Planets III*, eds. E. H. Levy, & J. I. Lunine, 1253
- Bailer-Jones, C. A. L., Rybizki, J., Fouesneau, M., Demleitner, M., & Andrae, R. 2021, *AJ*, **161**, 147
- Baraffe, I., Homeier, D., Allard, F., & Chabrier, G. 2015, *A&A*, **577**, A42
- Bate, M. R. 2000, *MNRAS*, **314**, 33
- Bate, M. R. 2018, *MNRAS*, **475**, 5618
- Bate, M. R., & Burkert, A. 1997, *MNRAS*, **288**, 1060
- Beuzit, J. L., Vigan, A., Mouillet, D., et al. 2019, *A&A*, **631**, A155
- Bohn, A. J., Ginski, C., Kenworthy, M. A., et al. 2021, *A&A*, **648**, A73
- Bonnell, I. A. 1994, *MNRAS*, **269**, 837
- Bonnell, I. A., & Bate, M. R. 1994a, *MNRAS*, **269**, L45
- Bonnell, I. A., & Bate, M. R. 1994b, *MNRAS*, **271**, 999
- Boss, A. P. 1997, *Science*, **276**, 1836
- Boss, A. P., & Bodenheimer, P. 1979, *ApJ*, **234**, 289
- Bowler, B. P., Blunt, S. C., & Nielsen, E. L. 2020, *AJ*, **159**, 63
- Brandt, T. D., Dupuy, T. J., Li, Y., et al. 2021, *AJ*, **162**, 186
- Burkert, A., Bate, M. R., & Bodenheimer, P. 1997, *MNRAS*, **289**, 497
- Canup, R. M., & Ward, W. R. 2002, *AJ*, **124**, 3404
- Chauvin, G., Lagrange, A. M., Dumas, C., et al. 2004, *A&A*, **425**, L29
- Claudi, R. U., Turatto, M., Gratton, R. G., et al. 2008, *SPIE Conf. Ser.*, **7014**, 70143E
- Crepp, J. R., Principe, D. A., Wolff, S., et al. 2018, *ApJ*, **853**, 192
- Dahlqvist, C. H., Milli, J., Absil, O., et al. 2022, *A&A*, **666**, A33
- dal Ponte, M., Santiago, B., Carnero Rosell, A., et al. 2023, *MNRAS*, **522**, 1951
- Davies, C. L. 2019, *MNRAS*, **484**, 1926
- De Rosa, R. J., Nielsen, E. L., Wahhaj, Z., et al. 2023, *A&A*, **672**, A94
- Delorme, P., Meunier, N., Albert, D., et al. 2017, in *SF2A-2017: Proceedings of the Annual meeting of the French Society of Astronomy and Astrophysics*, eds. C. Reylé, P. Di Matteo, F. Herpin, E. Lagarde, A. Lançon, Z. Meliani, & F. Royer, Di
- Desidera, S., Chauvin, G., Bonavita, M., et al. 2021a, *A&A*, **651**, A70
- Desidera, S., Chauvin, G., Bonavita, M., et al. 2021b, *VizieR Online Data Catalog: J/A+A/651/A70*
- Do Ó, C. R., O’Neil, K. K., Konopacky, Q. M., et al. 2023, *AJ*, **166**, 48
- Dohlen, K., Langlois, M., Saisse, M., et al. 2008, *SPIE Conf. Ser.*, **7014**, 70143L
- Dupuy, T. J., Liu, M. C., & Ireland, M. J. 2014, *ApJ*, **790**, 133
- Foreman-Mackey, D., Hogg, D. W., Lang, D., & Goodman, J. 2013, *PASP*, **125**, 306
- Franson, K., Bowler, B. P., Zhou, Y., et al. 2023, *ApJ*, **950**, L19
- Fusco, T., Rousset, G., Sauvage, J. F., et al. 2006, *Opt. Express*, **14**, 7515
- Galicher, R., Boccaletti, A., Mesa, D., et al. 2018, *A&A*, **615**, A92
- Geißler, K., Chauvin, G., & Sterzik, M. F. 2008, *A&A*, **480**, 193
- Gomez Gonzalez, C. A., Wertz, O., Absil, O., et al. 2017, *AJ*, **154**, 7
- Grandjean, A., Lagrange, A. M., Keppler, M., et al. 2020, *A&A*, **633**, A44
- Greaves, J. S., Kennedy, G. M., Thureau, N., et al. 2014, *MNRAS*, **438**, L31
- Guenther, E. W., Neuhäuser, R., Huéramo, N., Brandner, W., & Alves, J. 2001, *A&A*, **365**, 514
- Guyon, O., Bendek, E. A., Eisner, J. A., et al. 2012, *ApJS*, **200**, 11
- Holman, M. J., & Wiegert, P. A. 1999, *AJ*, **117**, 621
- Holmberg, J., Nordström, B., & Andersen, J. 2009, *A&A*, **501**, 941
- Houk, N., & Cowley, A. P. 1975, *University of Michigan Catalogue of two-dimensional spectral types for the HD stars. Volume I. Declinations -90\_ to -53\_f0.*
- Hurt, S. A., & MacGregor, M. A. 2023, *ApJ*, **954**, 10
- Iglesias, D. P., Panić, O., Rebollido, I., et al. 2023, *MNRAS*, **526**, 2500
- Keppler, M., Benisty, M., Müller, A., et al. 2018, *A&A*, **617**, A44
- Kervella, P., Arenou, F., & Thevenin, F. 2021, *VizieR Online Data Catalog: J/A+A/657/A7*
- Kervella, P., Arenou, F., & Thévenin, F. 2022, *A&A*, **657**, A7
- Kingma, D. P., & Ba, J. 2014, arXiv e-prints, [arXiv:1412.6980]
- Lagrange, A. M., Desort, M., Galland, F., Udry, S., & Mayor, M. 2009, *A&A*, **495**, 335
- Lagrange, A. M., Bonnefoy, M., Chauvin, G., et al. 2010, *Science*, **329**, 57
- Larson, R. B. 1972, *MNRAS*, **156**, 437
- Lazzoni, C., Desidera, S., Marzari, F., et al. 2018, *A&A*, **611**, A43
- Lazzoni, C., Zurlo, A., Desidera, S., et al. 2020, *A&A*, **641**, A131
- Lazzoni, C., Desidera, S., Gratton, R., et al. 2022, *MNRAS*, **516**, 391
- Lazzoni, C., Rice, K., Zurlo, A., Hinkley, S., & Desidera, S. 2024, *MNRAS*, **527**, 3837
- Lee, A. T., Offner, S. S. R., Kratter, K. M., Smullen, R. A., & Li, P. S. 2019, *ApJ*, **887**, 232
- Lowrance, P. J., Schneider, G., Kirkpatrick, J. D., et al. 2000, *ApJ*, **541**, 390
- Maire, A. L., Skemer, A. J., Hinz, P. M., et al. 2015, *A&A*, **576**, A133
- Maire, A.-L., Langlois, M., Dohlen, K., et al. 2016, *SPIE Conf. Ser.*, **9908**, 990834
- Maire, A.-L., Langlois, M., Delorme, P., et al. 2021, *J. Astron. Telescopes Instrum. Syst.*, **7**, 035004
- Mannings, V., & Barlow, M. J. 1998, *ApJ*, **497**, 330
- Marley, M. S., Fortney, J., Seager, S., & Barman, T. 2007, in *Protostars and Planets V*, eds. B. Reipurth, D. Jewitt, & K. Keil, 733
- Marois, C., Lafrenière, D., Doyon, R., Macintosh, B., & Nadeau, D. 2006, *ApJ*, **641**, 556
- Mawet, D., Milli, J., Wahhaj, Z., et al. 2014, *ApJ*, **792**, 97
- Mayor, M., & Queloz, D. 1995, *Nature*, **378**, 355
- Mayer, L., Quinn, T., Wadsley, J., & Stadel, J. 2004, *ApJ*, **609**, 1045
- Mesa, D., Gratton, R., Kervella, P., et al. 2023, *A&A*, **672**, A93
- Miret-Roig, N., Galli, P. A. B., Brandner, W., et al. 2020, *A&A*, **642**, A179
- Moré, J. J. 2006, in *Numerical analysis: proceedings of the biennial Conference held at Dundee, June 28–July 1, 1977* (Springer), 105
- Neuhäuser, R., Ginski, C., Schmidt, T. O. B., & Mugrauer, M. 2011, *MNRAS*, **416**, 1430

- Öberg, K. I., Murray-Clay, R., & Bergin, E. A. 2011, *ApJ*, **743**, L16
- Ochiai, H., Nagasawa, M., & Ida, S. 2014, *ApJ*, **790**, 92
- Offner, S. S. R., Dunham, M. M., Lee, K. I., Arce, H. G., & Fielding, D. B. 2016, *ApJ*, **827**, L11
- Offner, S. S. R., Moe, M., Kratter, K. M., et al. 2023, in *Astronomical Society of the Pacific Conference Series*, 534, Protostars and Planets VII, eds. S. Inutsuka, Y. Aikawa, T. Muto, K. Tomida, & M. Tamura, 275
- Pavlov, A., Möller-Nilsson, O., Feldt, M., et al. 2008, *SPIE Conf. Ser.*, **7019**, 701939
- Pearce, T. D., & Wyatt, M. C. 2014, *MNRAS*, **443**, 2541
- Pérez, S., Marino, S., Casassus, S., et al. 2019, *MNRAS*, **488**, 1005
- Petit, C., Sauvage, J. F., Fusco, T., et al. 2014, *SPIE Conf. Ser.*, **9148**, 914800
- Petrus, S., Whiteford, N., Patapis, P., et al. 2024, *ApJ*, **966**, L11
- Phillips, M. W., Tremblin, P., Baraffe, I., et al. 2020, *A&A*, **637**, A38
- Pollack, J. B., Hubickyj, O., Bodenheimer, P., et al. 1996, *Icarus*, **124**, 62
- Rameau, J., Chauvin, G., Lagrange, A. M., et al. 2013a, *ApJ*, **772**, L15
- Rameau, J., Chauvin, G., Lagrange, A. M., et al. 2013b, *A&A*, **553**, A60
- Ruffio, J.-B., Horstman, K., Mawet, D., et al. 2023, *AJ*, **165**, 113
- Schmid, H. M., Bazzon, A., Roelfsema, R., et al. 2018, *A&A*, **619**, A9
- Smith, R., Churcher, L. J., Wyatt, M. C., Moerchen, M. M., & Telesco, C. M. 2009, *A&A*, **493**, 299
- Soummer, R., Pueyo, L., & Larkin, J. 2012, *ApJ*, **755**, L28
- Szulágyi, J., Mayer, L., & Quinn, T. 2017, *MNRAS*, **464**, 3158
- Vousden, W. D., Farr, W. M., & Mandel, I. 2016, *MNRAS*, **455**, 1919
- Wertz, O., Absil, O., Gómez González, C. A., et al. 2017, *A&A*, **598**, A83
- Youngblood, A., Roberge, A., MacGregor, M. A., et al. 2021, *AJ*, **162**, 235
- Zhang, Z., Mollière, P., Hawkins, K., et al. 2023, *AJ*, **166**, 198
- Zúñiga-Fernández, S., Bayo, A., Elliott, P., et al. 2021, *A&A*, **645**, A30
- Zurlo, A., Vigan, A., Mesa, D., et al. 2014, *A&A*, **572**, A85
- Zurlo, A., Vigan, A., Galicher, R., et al. 2016, *A&A*, **587**, A57

Appendix A: Cornerplot of the orbital fitting

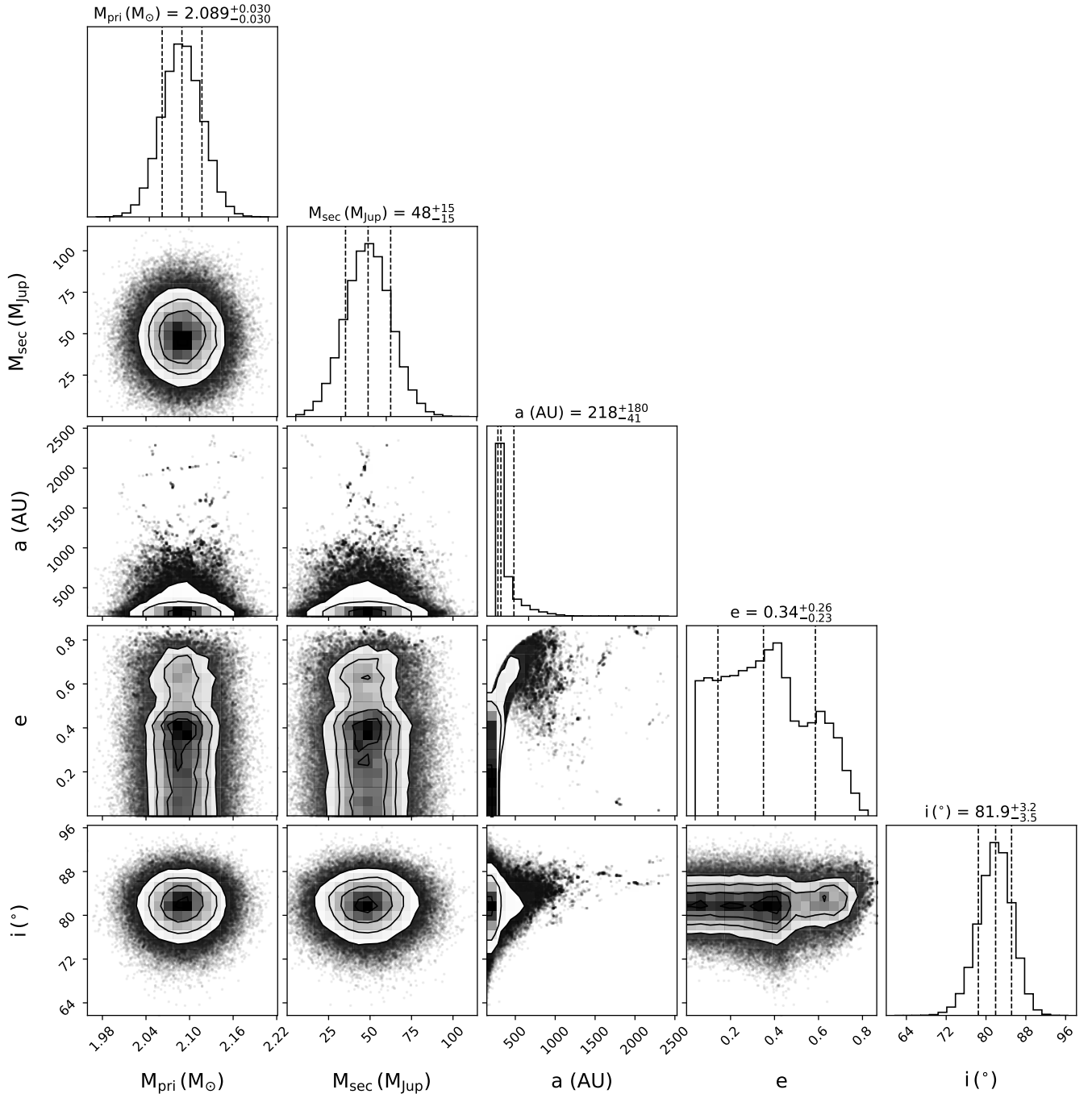


Fig. A.1: Corner plot showing the results of the orbital fitting performed by Orvara, after excluding orbits based on constraints described in Sec. 4.1. The best-fit values are also reported in Table 7.